Detection of significant cm to sub-mm band radio and γ-ray correlated variability in *Fermi* bright blazars

L. Fuhrmann,[1]$\star$ S. Larsson,[2] J. Chiang,[3] E. Angelakis,[1] J. A. Zensus,[1] I. Nestoras,[1] T. P. Krichbaum,[1] H. Ungerechts,[4] A. Sievers,[4] V. Pavlidou,[1] A. C. S. Readhead,[5] W. Max-Moerbeck[5] and T. J. Pearson[5]

[1] *Max-Planck-Institut für Radioastronomie, Auf dem Hügel 69, D-53121 Bonn, Germany*
[2] *Oskar Klein Centre, Department of Astronomy, Stockholm University, AlbaNova, SE-10691 Stockholm, Sweden*
[3] *W. W. Hansen Experimental Physics Laboratory, Kavli Institute for Particle Astrophysics and Cosmology, Department of Physics and SLAC National Accelerator Laboratory, Stanford University, Stanford, CA 94305, USA*
[4] *Institut de Radio Astronomie Millimétrique, Avenida Divina Pastora 7, Local 20, E-18012 Granada, Spain*
[5] *California Institute of Technology, Pasadena, CA 91125, USA*

ABSTRACT

The exact location of the γ-ray emitting region in blazars is still controversial. In order to attack this problem we present first results of a cross-correlation analysis between radio (11 cm to 0.8 mm wavelength, F-GAMMA programme) and γ-ray (0.1–300 GeV) $\sim$3.5 yr light curves of 54 *Fermi*-bright blazars. We perform a source stacking analysis and estimate significances and chance correlations using mixed source correlations. Our results reveal: (i) the first highly significant multiband radio and γ-ray correlations (radio lagging γ rays) when averaging over the whole sample, (ii) average time delays (source frame: 76 ± 23 to 7 ± 9 d), systematically decreasing from cm to mm/sub-mm bands with a frequency dependence $\tau_{r, \gamma}(\nu) \propto \nu^{-1}$, in good agreement with jet opacity dominated by synchrotron self-absorption, (iii) a bulk γ-ray production region typically located within/upstream of the 3 mm core region ($\tau_{3mm, \gamma} = 12 \pm 8$ d), (iv) mean distances between the region of γ-ray peak emission and the radio '$\tau = 1$ photosphere' decreasing from 9.8 ± 3.0 pc (11 cm) to 0.9 ± 1.1 pc (2 mm) and 1.4 ± 0.8 pc (0.8 mm), (v) 3 mm/γ-ray correlations in nine individual sources at a significance level where one is expected by chance (probability: 4×10^{-6}), (vi) opacity and 'time lag core shift' estimates for quasar 3C 454.3 providing a lower limit for the distance of the bulk γ-ray production region from the supermassive black hole (SMBH) of $\sim$0.8–1.6 pc, i.e. at the outer edge of the broad-line region (BLR) or beyond. A 3 mm $\tau = 1$ surface at $\sim$2–3 pc from the jet base (i.e. well outside the 'canonical BLR') finally suggests that BLR material extends to several parsec distances from the SMBH.

Key words: galaxies: active – galaxies: jets – galaxies: nuclei – quasars: general – gamma-rays: galaxies – radio continuum: galaxies.

1 INTRODUCTION

Since the era of the Energetic Gamma-ray Experiment Telescope (EGRET) on-board the Compton Gamma-ray Observatory, the relation between the γ-ray and radio emission in active galactic nuclei (AGN) has been intensively discussed. In particular, the location of the γ-ray production and dissipation region in AGN jets is still a matter of active debate – recently re-activated and intensified thanks to the Large Area Telescope (LAT) on board the *Fermi Gamma-*

ray Space Telescope (*Fermi*). The LAT is a pair-conversion γ-ray telescope sensitive to photon energies from about 20 MeV up to >300 GeV. Due to its unprecedented sensitivity and all-sky monitoring capabilities, *Fermi*/LAT is providing for the first time γ-ray light curves and spectra resolved at a variety of time-scales for a large number ($\sim$10^3) of AGN since its launch in 2008 (e.g. Abdo et al. 2010b; Ackermann et al. 2011).

Different theoretical models and observational findings suggest different locations of the γ-ray emitting region, either at (i) small distances from the central supermassive black hole (SMBH), i.e. inside the broad-line region (BLR, sub-parsec) or even within a few 100 Schwarzschild radii, very close to the accretion disc

$\star$ E-mail: lfuhrmann@mpifr-bonn.mpg.de

(e.g. Blandford & Levinson 1995) or (ii) at larger distances, e.g. in regions of radio shocks, shock–shock interaction, in various jet layers or turbulent cells parsecs downstream of the jet (e.g. Valtaoja & Teräsranta 1995; Marscher & Jorstad 2010; Schinzel et al. 2012; Marscher 2014). The knowledge of the γ-ray emission location, however, is of great importance for any model trying to explain the origin of the processes responsible for bulk γ-ray photon production and energy dissipation (e.g. Ghisellini & Tavecchio 2009; Dermer et al. 2014). In leptonic models, for instance, the exact location of the dissipation region constrains the origin of the main seed photon fields available for inverse Compton (IC) up-scattering to high energies, i.e. either accretion disc/BLR/jet synchrotron photons ($\lesssim$1 pc) or dust torus and/or jet synchrotron photons ($\gtrsim$1 pc).

Observationally, several findings disfavour the 'large distance' scenario, for instance: (i) rapid ($\leq$hours) MeV/GeV variability observed in a few sources (e.g. Foschini et al. 2010; Tavecchio et al. 2010; Rani et al. 2013b) suggests ultracompact emission regions and, assuming that the emission region is taking up the entire jet cross-section in a conical jet geometry, a location not too far from the central engine; (ii) the high-energy spectral breaks observed by *Fermi* have been interpreted as γ-ray photoabsorption via He II Lyman recombination in the BLR (Poutanen & Stern 2010; Stern & Poutanen 2011), (iii) spectral-energy distribution modelling can often describe well the high-energy emission within leptonic scenarios by external Compton scattering of seed photons from the BLR and/or accretion disc (e.g. Finke & Dermer 2010).

On the other hand, detailed multiwavelength studies of single sources including cross-band (radio, optical, X-ray, γ-ray and polarization) and relative timing analysis of outbursts and/or very long baseline interferometry (VLBI) component ejection/kinematics suggest relativistic shocks, shock–shock interaction and/or multiple jet regions on parsec scales as sites of the γ-ray emission (e.g. Jorstad et al. 2001, 2010; Marscher et al. 2010; Agudo et al. 2011b; Schinzel et al. 2012; Orienti et al. 2013; Raiteri et al. 2013; Rani et al. 2013a). For instance, the joint occurrence of a γ-ray flare and an optical polarization position angle swing observed in 3C 279 provides evidence for cospatial emission regions along a curved trajectory at a significant distance from the central engine (Abdo et al. 2010a). Similarly, joint γ-ray and mm-band flares and (mm/optical) polarization peaks along with jet kinematics also suggest cospatial emission regions many parsecs downstream of the jet in OJ 287 (Agudo et al. 2011a). Finally, rapid variability on time-scales of minutes in the few hundred GeV to TeV energy range cannot be produced within the BLR due to high pair production γ-ray opacity (e.g. Böttcher, Reimer & Marscher 2009; Tavecchio & Ghisellini 2012).

Dotson et al. (2012) presented a new method to locate the energy dissipation region via the energy dependent decay times of flares in the different cooling regimes of the BLR (Klein–Nishina regime) and the parsec-scale molecular torus region (Thomson regime). However, this method is limited to the most powerful γ-ray events providing enough photon statistics to detect significant differences in *Fermi* light curves at two different energy bands. Alternatively, detailed multiwavelength and cross-correlation studies of large samples are capable of providing additional constraints on the location of the γ-ray emitting region. For instance, different studies aim at detecting time delays between γ rays and 15 GHz radio single dish as well as long-term VLBI data of large samples (e.g. Pushkarev, Kovalev & Lister 2010; Max-Moerbeck et al. 2013), indicating that cm-band radio flares are generally delayed w.r.t. γ rays (see also Kovalev et al. 2009). Parsec-scale distances have been inferred from delays of γ-ray peak emission w.r.t. 37 GHz radio flare onsets in a

sample of sources monitored by the Metsähovi group (León-Tavares et al. 2011), in line with earlier results of similar studies conducted during the EGRET era (e.g. Lähteenmäki & Valtaoja 2003).

Here, we present the first results of a cross-correlation analysis of a larger blazar sample based on multifrequency radio (cm, mm and sub-mm wavelengths) light curves obtained by the F-GAMMA programme (e.g. Fuhrmann et al. 2007, 2014) and ~3.5 yr γ-ray light curves of 54 *Fermi*-bright blazars. The study aims at (i) establishing statistically significant correlations between the radio and γ-ray bands in a sample average sense by estimating correlation significances and chance correlations using mixed source correlations as well as a cross-correlation stacking analysis and (ii) further constraining the location of the γ-ray emitting region in these sources. The paper is structured as follows. In Section 2 the sample and data sets are introduced. Section 3 describes the applied cross-correlation methods and analysis, whereas Sections 4 and 5 present and discuss the results. A summary and concluding remarks are given in Section 6.

2 THE SOURCE SAMPLE AND DATA SETS

2.1 The F-GAMMA programme: cm to sub-mm band light curves

The cm, mm and sub-mm band radio data used for the current study have been collected in the framework of the *Fermi* related F-GAMMA monitoring programme (Fuhrmann et al. 2007, 2014; Angelakis et al. 2010). Since 2007, the F-GAMMA programme has been monitoring contemporaneously the total flux density, polarization and spectral evolution of about 60 *Fermi* blazars at three radio observatories, enabling detailed AGN studies of broad-band variability, emission processes as well as the radio/γ-ray connection. The overall wavelength range spans 110 to 0.8 mm (2.64 to 345 GHz) using the Effelsberg (EB) 100 m, IRAM 30 m (at Pico Veleta, PV) and Atacama Pathfinder EXperiment (APEX) 12 m telescopes at a total of 11 bands (see Table 1). The monthly observations at EB and PV are performed quasi-simultaneously (typically within days) and in a highly synchronized manner together with the more general flux monitoring conducted at the IRAM 30 m telescope. APEX sub-mm observations are performed for 25 F-GAMMA sources in addition to a sample of interesting Southern hemisphere *Fermi*-detected AGN not observable from the EB and PV sites.

The Effelsberg measurements were conducted with cross-scans using the secondary focus heterodyne receivers at eight wavebands between 110 and 7 mm wavelength (2.64 to 43.00 GHz, see Table 1). The IRAM 30 m observations were carried out with calibrated cross-scans using the 'B' and 'C' SIS (until 2009 March) and Eight Mixer Receiver (EMIR) heterodyne receivers

Table 1. Summary of the different wave/energy bands used in the current analysis.

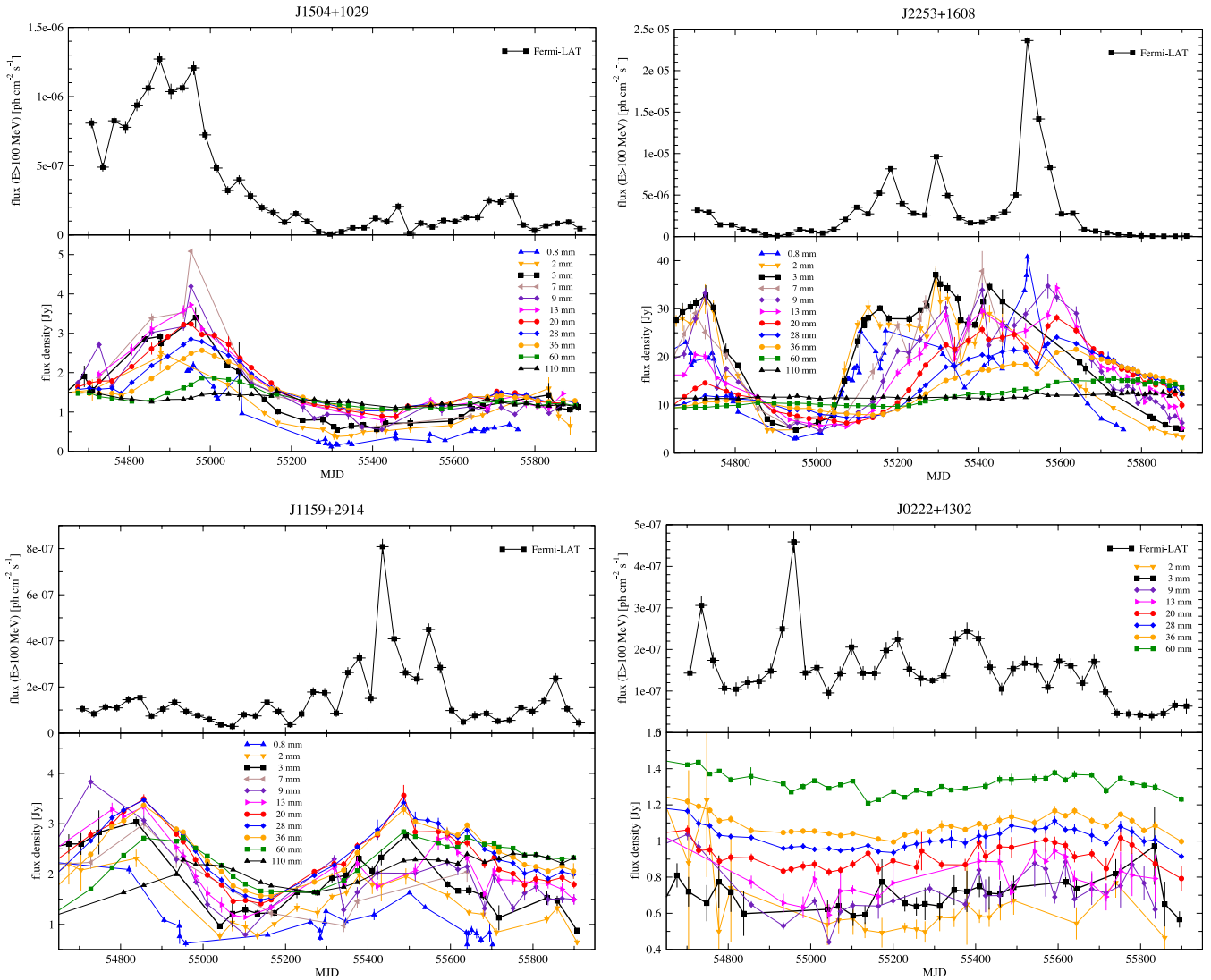| Facility (F-GAMMA)	Band (mm)	Frequency (GHz)	Energy (GeV)
Effelsberg 100 m	110, 60, 36	2.64, 4.85, 8.35	–
	28, 20, 13	10.45, 14.6, 23.05	–
	9, 7	32.0, 43.0	–
IRAM 30 m	3, 2	86.2, 142.3	–
APEX 12 m	0.8	345	–
Fermi/LAT	–	–	0.1–300

Figure 1. The γ-ray (top) and radio (bottom) light curves (flux versus modified Julian date, MJD) for four selected, bright γ-ray sources of the studied sample: J1504+1029 (PKS 1502+106, top left; redshift: 1.84), J2253+1608 (3C 454.3, top right; redshift: 0.86), J1159+2914 (4C 29.45, bottom left; redshift: 0.73) and J0222+4302 (3C 66A, bottom right; redshift: 0.44). The top two and bottom left sources demonstrate cases of possible correlations between both bands, whereas no correlated variability is evident for J0222+4302 (bottom right).

operating at 3 and 2 mm wavelengths (86.2 and 142.3 GHz). Finally, the Large Apex Bolometer Camera (LABOCA) array was used at APEX operating at a wavelength of 0.87 mm (345 GHz). In the data reduction process for each station, pointing offset, gain elevation, atmospheric opacity and sensitivity corrections have been applied to the data. The details of the programme, observations and data reduction are described in Fuhrmann et al. (2014) and Larsson et al. (2012, see also Fuhrmann et al. 2008; Angelakis et al. 2010, in preparation; Nestoras et al., in preparation). Example light curves of four selected sources (J0222+4302, J1159+2914, J1504+1029 and J2253+1608) including all radio bands are shown in Fig. 1. The data of J0222+4302 (3C 66A) at 110 mm wavelength are affected by the close-by radio galaxy 3C 66B and thus have been omitted.

2.2 The source sample

The present study is focusing on the sources observed at radio bands by the F-GAMMA monitoring programme. With a total of about 90 AGN/blazars ever observed since 2007 January, these

sources constitute a sample of well known, frequently active and bright blazars ($\delta > -30°$) for detailed studies of the *most prominent* behaviour of the *brightest* γ-ray-loud blazars.

For the particular analysis presented here we selected a subsample from the above F-GAMMA sources according to the following criteria. (i) *Fermi*-detection: presence in the First Fermi/LAT catalogue, (ii) 'best suitable' radio light curves: sources with the best frequency and time coverage that are well sampled over the considered *Fermi* time period of about 3.5 yr and (iii) presence of radio variability: sources showing significant variability on the basis of a χ^2 test.

This selection results in a subsample of 54 sources comprised of 35 flat-spectrum radio quasars (FSRQs), 18 BL Lacertae objects (BL Lacs) and one narrow-line Seyfert 1 galaxy. Table 2 presents the complete list of selected sources. At the sub-mm band the selected subsample is slightly different due to the different source sample observed at the APEX telescope. In this case, a total of 38 sources have been selected, including (i) 23 sources of the above subsample of 54 sources and (ii) 15 additional, Southern hemisphere

Table 2. List of selected sources included in the current analysis (see the text for details).

Source	2FGL name	Other name	Type
J0050−0929	J0050.6−0929	PKS 0048−097	BL Lac
J0102+5824	J0102.7+5827	TXS 0059+581	FSRQ
J0136+4751	J0136.9+4751	OC 457	FSRQ
J0217+0144	J0217.9+0143	PKS 0215+015	FSRQ
J0222+4302	J0222.6+4302	3C 66A	BL Lac
J0237+2848	J0237.8+2846	4C +28.07	FSRQ
J0238+1636	J0238.7+1637	AO 0235+164	BL Lac
−			

Note. This table is available in its entirety as online material.

Fermi-detected AGN also satisfying the above criteria. The latter are given at the bottom of Table 2 .

Given our source selection and the resulting statistical incompleteness of the studied sample, we note that the results presented in the following may not be representative of the AGN/blazar population in its entirety.

2.3 *Fermi γ*-ray light curves

The *Fermi γ*-ray light curves for the studied sample have been produced in a pipeline fashion using time boundaries to best match the radio light curves: a 28-d binning starting on 2008 August 15 and ending on 2012 January 26 was used. The choice of 28-d binning was primarily driven by the predetermined cadence of the F-GAMMA radio light curves (about one month). Furthermore, this choice is also a trade-off between time resolution and good signal-to-noise ratio in each time bin for low *γ*-ray flux states and/or weaker sources in the sample.

The source model for each *region-of-interest* (ROI) containing the target sources included nearby point sources, determined from the Second *Fermi*/LAT (2FGL) catalogue (Nolan et al. 2012), and the standard Galactic and isotropic diffuse emission models (two year P7V6 models[1]). The latter component includes contributions from unresolved extragalactic emission and any residual charged particle backgrounds. A maximum likelihood analysis of each ROI was performed with SCIENCETOOLS version 09-26-00, and the P7SOURCE_V6 instrument response functions. The fluxes and photon spectral indices were fit for each target source assuming a single power law over the energy range 0.1–300 GeV. Examples of the *γ*-ray light curves are shown in Fig. 1. We note that due to the 28-d binning interval, more rapid *γ*-ray flares and variability on time-scales of hours/days to a few weeks is smoothed out and not resolved with our data sets.

In total, *Fermi γ*-ray light curves were produced for 131 sources. In addition to our studied sample of 54 sources, we included 77 reference blazars with good quality *Fermi* light curves that were used for estimating correlation significances, as described in Section 3. The reference sources were chosen among the brightest blazars in the Second *Fermi*/LAT AGN catalogue (2LAC; Ackermann et al. 2011), including sources of each blazar type (FSRQs; low, intermediate and high synchrotron peaked BL Lacs). Their *γ*-ray light curves were produced in the same way as the light curves for our sample of 54 target sources.

3 CROSS-CORRELATION ANALYSIS

3.1 The DCCF method

In order to search for possible correlations between the *γ*-ray and radio light curves, we use a cross-correlation analysis. For two discrete, evenly sampled light curves, $x(t_i)$ and $y(t_i)$, the cross-correlation function (CCF) as function of time lag τ is defined as

$$\text{CCF}(\tau) = \frac{1}{N} \sum_{i=1}^{N} \frac{[x(t_i) - \bar{x}][y(t_i - \tau) - \bar{y}]}{\sigma_x \sigma_y}, \tag{1}$$

with $\bar{x}$, σ_x and $\bar{y}$, σ_y being the mean and standard deviation of $x(t_i)$ and $y(t_i)$, respectively. Given the uneven sampling of the light curves considered here, we in particular use a discrete cross-correlation function (DCCF) analysis (Edelson & Krolik 1988), where in contrast to linear interpolation methods, the contribution to the CCF is calculated only using the actual data points. Each pair of points, one from each of the two light curves, then provides one correlation value at a lag corresponding to their time separation. For two light curves with N and M data points, respectively, this gives an unbinned cross-correlation function (UCCF)

$$\text{UCCF}_{ij} = \frac{(x_i - \bar{x})(y_j - \bar{y})}{\sigma_x \sigma_y}. \tag{2}$$

The DCCF is then obtained by averaging the UCCF in time lag bins. For light curves exhibiting stationary variability, the mean and variance is the same for different parts of the data, except for statistical fluctuations. For non-stationary light curves the mean and variance may exhibit larger fluctuations and in order to take this into account it is advantageous to calculate a new mean and variance for each time lag bin, using only the data points that contribute to the DCCF at that lag (see White & Peterson 1994). With this definition the value of the DCCF is identical to Pearson's r-statistic. Values can vary between −1 and +1. A positive value implies correlated variability and a negative value corresponds to an anticorrelation. A DCCF peak at some time lag τ implies, in case it is significant (see Section 3.2), correlated variability with an average time shift τ between the two time series. In all our analysis positive lag denotes *γ*-ray leading radio. For each source, DCCFs were calculated between the *γ*-ray light curve and each of the radio light curves (0.8, 2, 3, 9, 7, 13, 20, 28, 36, 60 and 110 mm wavelength). Examples of 3 mm/*γ*-ray DCCFs for four single sources are shown in Fig. 2. For instance, the DCCF of J1504+1029 (top left) shows a clear positive peak in the DCCF with amplitude close to 1 at a small positive time lag τ indicating correlated variability with 3 mm radio lagging behind *γ* rays by a certain time lag. In contrast, J0222+4302 (bottom left) shows no prominent, positive or negative DCCF peak. Hence, no correlation between the two bands is detected over the time period of about 3.5 yr.

To estimate the location and time lag of each DCCF peak, we fit a Gaussian function over a lag range of 200 d for the short wavelength bands ($\leq$3 mm) to 300 d for the longer wavelengths ($\geq$7 mm). Uncertainties were estimated by a model independent Monte Carlo method (Peterson et al. 1998) accounting for the effects of measurement noise and data sampling. The Monte Carlo run consisted of a bootstrap selection of a subsample of data points in each light curve plus injection of white noise with a standard deviation equal to the error value at each data point. The uncertainties in correlation time lags are then estimated as the standard deviations of peak fits to these simulations.
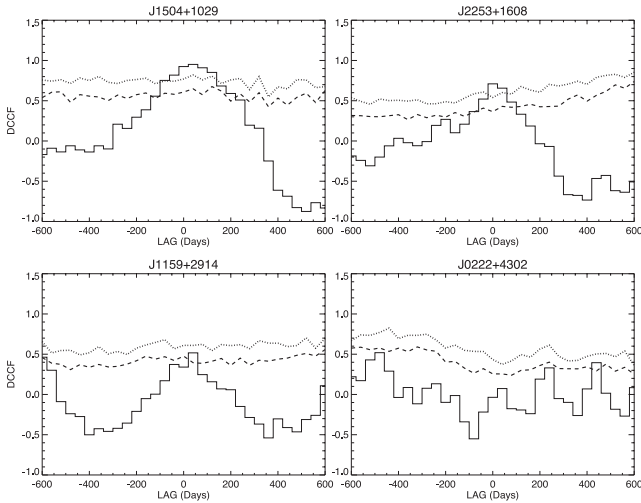
Figure 2. 3 mm/γ-ray DCCFs (observers frame) of the single sources also shown in Fig. 1, namely J1504+1029 (top, left), J2258+1608 (top, right), J1159+2914 (bottom, left) and J0222+4302 (bottom, right), with 99 per cent (dotted lines) and 90 per cent (dashed lines) significance levels superimposed. Only the top two cases show significant correlations above 99 per cent significance.

3.2 Correlation significance: mixed source correlations

The strength and significance of peaks seen in the DCCF depends on the stochastic nature of the variability, the correlation properties, the data sampling, the measurement noise and the total length of the time series. The latter limits the number of observed events for a given source which furthermore depends on the source duty cycle and the time-scale of the observed variability. For the data used in the present study, the correlation significance is primarily limited by chance correlations, i.e. DCCF peaks coming from physically unrelated variability in the two different spectral bands. If, for instance, the two light curves contain flares at times that are unrelated to each other, a correlation peak will be seen in the DCCF at a lag corresponding to their time separation even if they are causally unrelated. If the number of flares or variability features in the light curves are small these effects can be strong.

In order to estimate the probability that observed correlations are produced by chance correlations or observational effects we compute 'mixed source correlations'. This is done by correlating the radio light curve for a given source with all other 130 available γ-ray light curves in the same manner as described in Section 3.1 and then compare, for each lag bin, the distribution of these correlation values with the actual DCCF value of the source at the same lag. Under the assumption that the variability properties are similar for the different sources, the probability distribution of the resulting DCCFs reflect the occurrence of spurious correlations. The assumption of similar variability properties is supported by the fact that the 131 γ-ray light curves all show significant variability and are largely dominated by red noise like processes as demonstrated by a power spectral density analysis. The latter is in good agreement with previous findings of Ackermann et al. (2011) using 1 month binned, 2 year *Fermi* light curves of 156 FSRQs and 59 BL Lacs (including a large fraction of our sources).

Further details on the correlation techniques and significance estimates are given in Larsson (2012).

3.3 DCCF stacking analysis

With the present data our analysis is able to reveal significant correlations for a handful of sources as described in the next section. However, the sensitivity for the detection of correlations and their multifrequency properties as well as the DCCF peak significance can be largely improved by using the whole source sample. For that reason we perform a joint, or stacking, analysis and we do so in two different ways: (i) we simply average the DCCFs of all the sources, (ii) we first normalize the light curves by dividing with the mean flux density for each source and then include the contribution of all correlation data pairs in the computation of an average DCCF. The two methods give similar, but not identical results. In particular, the second method gives more weight to sources with large variability and to source light curves with a higher density of data points. The correlation significance is again estimated by mixed source correlations that are stacked in a similar way as the real source DCCFs. Each mixed source DCCF is only used once, which results in 130 stacked comparison DCCFs.

In the last part of the analysis we quantify how the correlation depends on radio wavelength. Here, we also take into account the cosmological time stretch by scaling time values with a factor of $1/(1 + z)$, such that the computed time lags refer to source rest frame. We note that in the current work we do not take into account that time values (time-scales and time lags) are additionally modified (shortened) by relativistic boosting effects ('jet rest frame'). This aspect will be addressed in a subsequent analysis (Larsson et al., in preparation).

The same 54 sources (mean redshift: 0.9) were used for each one of the 2–110 mm/γ-ray band combination, except for one source (J1626−2948) which was excluded from the 7–110 mm band DCCFs due to poor sampling. For the 0.8 mm DCCF, 38 APEX light curves were used, out of which 23 sources were also in the F-GAMMA sample used for the longer wavelengths.

4 RESULTS

Since the different radio bands are usually correlated (both in sampling and variability) and radio/γ-ray correlations are expected to be more pronounced towards shorter wavelengths (e.g. Fuhrmann et al. 2014), we only consider one radio band (3 mm) in order to establish the correlation significance. We choose the 3 mm band as being our best data set at short wavelengths in terms of sampling and measurement noise. We first present the results of the stacking analysis in Section 4.1, whereas the most significant single-source correlations of our analysis are reported in Section 4.2. In Section 4.3 we investigate how the average correlation depends on radio wavelength using the stacked DCCFs.

4.1 Correlation significance in stacking analysis

A 3 mm/γ-ray source averaged DCCF was calculated with each one of the two stacking methods described in Section 3.3. Both methods give a highly significant detection of correlated variability as can be seen in the top panel of Fig. 3, where the two DCCFs are shown together with 90 and 99 per cent significance levels as estimated from the mixed source correlations. The second stacking method (building the DCCF by adding data point pairs) results in a correlation peak DCCF$_{max}$ of 0.38 compared to 0.31 for the direct averaging of the individual source DCCFs. In both cases the
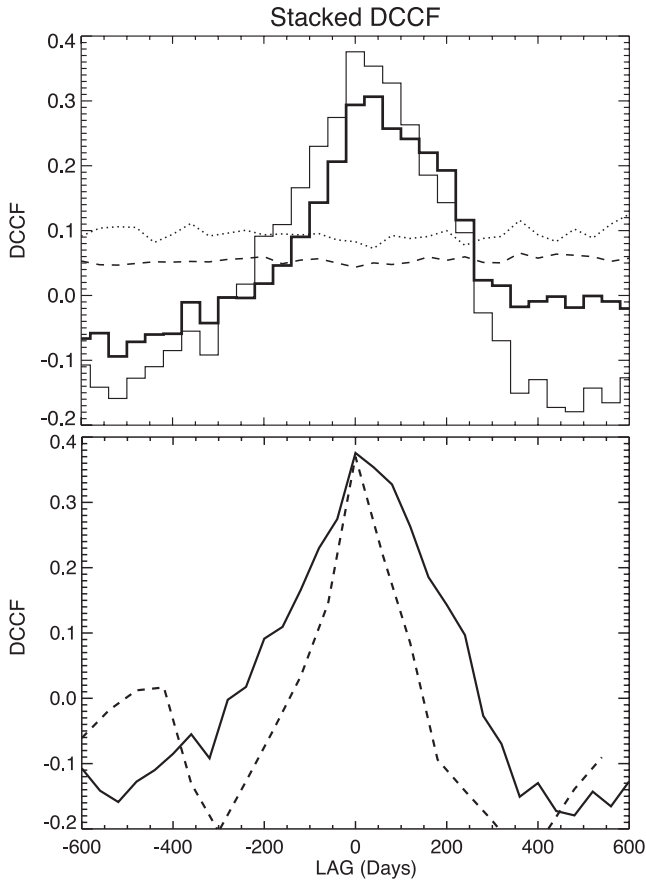
Figure 3. Averaged 3 mm/γ-ray DCCFs obtained from the stacking analysis. Top: DCCFs (observers frame) of both averaging methods are shown (bold line: direct averaging of DCCFs, see the text). 99 (dotted line) and 90 per cent (dashed line) significance levels for the direct averaging method are superimposed demonstrating the detection of highly significant correlations. Bottom: comparison of the stacked DCCFs obtained with (source frame, dashed line) and without (observers frame, solid line) redshift correction.

DCCF peak (average for lag -100 to $+100$ d) is more than eight times higher than the strongest of the mixed source DCCF used for comparison. We note that even after removing the 12 sources with the strongest correlations from the analysis, the DCCF correlation is still highly significant. In this case the average for the lag range -100 to $+100$ d still exceeds the strongest corresponding mixed source DCCF by a factor of 4. This demonstrates that the overall correlation is not restricted to or dominated by just a small fraction of the sources.

The correlation peak in the stacked DCCF of Fig. 3 (top) is broad and extends over a positive *and* negative lag range of several hundred days. This width is partly the result of the distribution of correlation lags among our sources, including the redshift effect (see the bottom panel of Fig. 3) and the possible presence of multiple lags in individual sources, but mostly it is an effect of the variability time-scale (see also Section 4.3). If the length of a γ-ray flaring period is longer than the time delay of the radio flare onset, the later part of the γ-ray flare will correlate with the beginning of the radio flare at a negative time lag. This is the main reason why the DCCF peak extends to negative lags – consistent with our findings of single sources not showing significant negative time lags (see Section 4.2).

4.2 Single sources: light curves and 3 mm/γ-ray DCCFs

The example light curves presented in Fig. 1 demonstrate the typical behaviour seen in the studied sample of 54 sources. A visual inspection of all light curves shows that (i) strong flux density outbursts (time-scales of months) and extended periods of activity (months to 1–2 yr) occur at both radio and γ rays, although single γ-ray events usually appear to be more rapid, (ii) the flaring activity is often characterized by significant substructure with faster subflares superimposed, in particular at γ-rays, (iii) the flaring activity often seems to happen quasi-simultaneously at both bands, i.e. during periods of γ-ray activity the radio bands are correspondingly in an increasing or high flux/activity state, (iv) often obvious time lags (radio lagging) are evident between the peaks of radio and γ-ray flares, in particular towards longer radio wavelengths. The sources J1504+1029 and J2253+1608 shown in Fig. 1 are typical examples of the described characteristics. On the other hand, we identify several sources, like J0222+4302 (see Fig. 1), showing no obvious correlation. Despite substantial flaring activity at γ rays, there is no obvious corresponding variability at radio bands. Occasionally we also find (i) strong (factor $\sim$3–4) outbursts in one band with only a very mild 'counterpart' at the other spectral band, (ii) very rapid variability and flares in both bands without obvious, simple 'one-to-one' correspondences of events. Finally, we find evidence that the mm/sub-mm band flux density rises simultaneously with or even before the γ rays in a few cases.

The examples of 3 mm/γ-ray DCCFs for individual sources shown in Fig. 2 confirm the impression of correlated variability in the light curves of the first two cases (J1504+1029 and J2253+1608): a prominent peak close to zero lag and above our significance levels is seen. In contrast, no DCCF peak is seen in the case of J0222+4302. In the case of J1159+2914 we find a prominent DCCF peak close to zero lag, though well below the 99 per cent significance level.

The 90 and 99 per cent significance levels shown in Fig. 2 refer to individual time bins in the DCCF and are estimated from comparisons with the mixed source correlations. Based on the strong and well-defined correlation peak seen in the 3 mm/γ-ray stacked DCCF of the whole sample, we compared, for each individual source, the DCCF level for the lag range from -100 to $+140$ d with the corresponding level for the 130 mixed source DCCFs. In 5 out of 54 sources the DCCF level exceeds all 130 comparison DCCFs (corresponding to a significance $>$99 per cent) and for another four sources the level is exceeded by 1 or 2 comparison DCCFs (significance $\gtrsim$98 per cent). Statistically we would expect about one case occurring by chance. The chance probability to obtain 9 cases or more is only 4×10^{-6}. These 9 sources with the most significant correlations are listed in Table 3 along with their estimated 3 mm/γ-ray time lag $\tau_{3\,mm,\gamma}$ (source frame). The estimated lags range between -4 ± 10 and 93 ± 16 d with a mean and median value of 28 and 15 d, respectively.

Radio/γ-ray light curve cross-correlations and time lags have been reported previously for a few sources of Table 3. In the case of J2202+4216 (BL Lacertae), Raiteri et al. (2013) estimated a lag of $\sim$120–150 d (observers frame) with the mm-bands lagging γ rays. As seen in Table 3, our analysis confirms a correlation in this source, though with a shorter lag of $\sim$100 d (observers frame). We note, however, that the analysis of Raiteri et al. (2013) covered a significantly longer time period (up to 2012 October 31) including the latest high activity period of BL Lacertae during 2012. Wehrle et al. (2012, see also Jorstad et al. 2013) reported a significant correlation with time lags close to zero using 1.3 mm Submillimeter Array

Table 3. Single sources showing the most significant 3 mm/γ-ray correlations. Source type, estimated time lag $\tau_{3\,mm,\gamma}$ (source frame), DCCF peak and $\Delta r_{3\,mm,\gamma}$ are given (see the text). Positive lag denotes γ-ray leading radio. For J0050−0929 no β_{app} was available to estimate θ and $\Delta r_{3\,mm,\gamma}$. An estimate for J0238+1636 has been omitted (see the text).

Source	Type	Lag (d)	$DCCF_{max}$	$\Delta r_{3\,mm/\gamma}$ (pc)
J0050−0929	BL Lac	48 ± 26	0.88 ± 0.09	–
J0237+2848	FSRQ	40 ± 10	0.90 ± 0.13	3.6
J0238+1636	BL Lac	− 4 ± 10	1.00 ± 0.17	–
J0530+1331	FSRQ	10 ± 8	0.82 ± 0.06	0.3
J1504+1029	FSRQ	14 ± 11	0.96 ± 0.05	2.1
J1733−1304	FSRQ	29 ± 26	0.85 ± 0.13	15.9
J2147+0929	FSRQ	15 ± 15	0.82 ± 0.09	0.2
J2202+4216	BL Lac	93 ± 16	0.82 ± 0.10	4.7
J2253+1608	FSRQ	8 ± 12	0.73 ± 0.06	0.9

(SMA) and *Fermi* γ-ray light curves of J2253+1608 (3C 454.3) up to 2011 October (i.e. comparable to our time range). As seen in Fig. 2 and Table 3, our analysis confirms this result. The estimated time lags are in good agreement given the lag uncertainties and the shorter observing wavelength of the SMA data. Agudo et al. (2011b) found significant correlations between γ rays and cm/mm bands for the prominent flaring activity of J0238+1636 (AO 0235+164) during the early phase of the *Fermi* mission (2008 August). The 1.3 mm/γ-ray DCCF of these authors is broad with peaks at lags ∼0 and ∼50 d (γ-ray leading). We stress that due to the 28-d binning interval our γ-ray light curve does not resolve the rising part of this flare which adds an additional systematic uncertainty. Consequently, given the differences in time range, sampling and time binning with respect to our analysis it is difficult to make a quantitative comparison of these results. We do note, however, that there is a qualitative agreement between the lag estimates of these studies.

As seen in Table 3, we do not find sources exhibiting a significant negative time lag, i.e. no significant case of 3 mm leading the γ rays is found. As is demonstrated by our stacking analysis, the low detection rate of significant single-source correlations does not imply the non-existence of correlations in the majority of single sources. While several cases like J0222+4302 in Fig. 2 are present, the low detection rate is primarily induced by the limited time span of 3.5 yr, i.e. the so far limited statistics and small number of available events for single sources. Here, longer data trains will significantly improve the situation. A detailed single-source analysis using 5 yr data sets is in progress (Fuhrmann et al., in preparation). Furthermore, Table 3 shows that the current analysis reveals significant single-source correlations for both FSRQs and BL Lacs in the sample. This motivates future studies of stacked correlations separated by source type to search for possible differences in correlation behaviour (correlation strength, time lags etc.; Larsson et al., in preparation).

4.3 Stacked DCCF as a function of wavelength

Having established the presence of a highly significant 3 mm/γ-ray correlation in the stacked analysis we now repeat the analysis for each of the radio bands.

In Fig. 4 the average DCCFs for all radio/γ-ray combinations are presented. The first thing to be noticed is an increase in DCCF width towards longer cm bands. In particular, an asymmetric DCCF shape is seen with a wing extending to larger radio lags and becoming more pronounced towards 110 mm wavelength, consistent with the
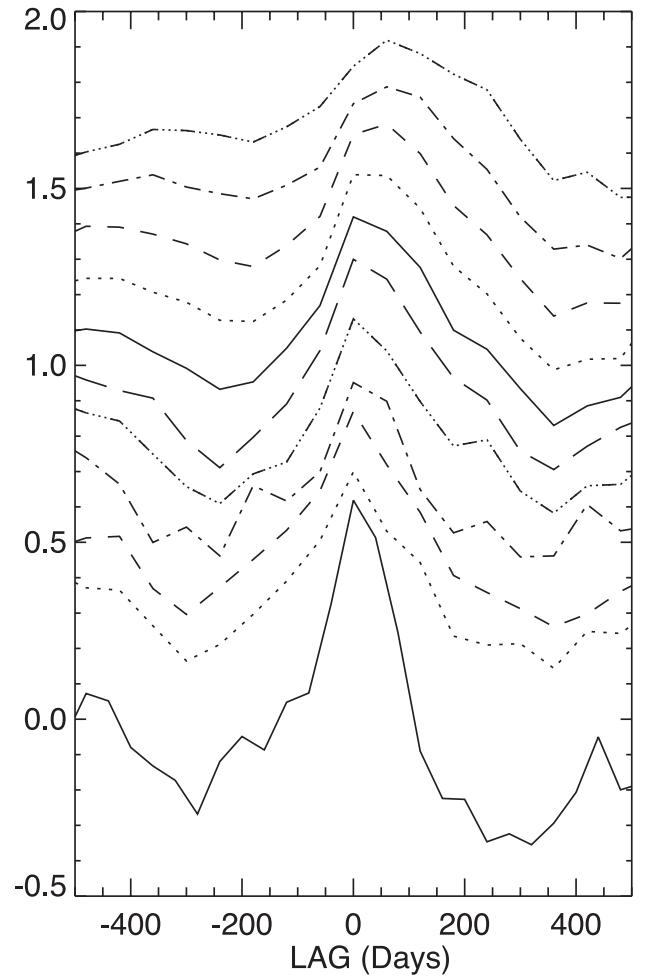

Figure 4. Stacked radio/γ-ray DCCFs (source frame) across all radio bands. From top to bottom are shown: γ-ray versus 110, 60, 36, 28, 20, 13, 9, 7, 3, 2 and 0.8 mm wavelength. For better illustration, the 2 mm/γ-ray DCCF has been displaced along the *y*-axis by 0.35 and the longer radio wavelength ones each by an additional shift of 0.15. Since time values are redshift corrected, fewer data points contribute to the stacked DCCF at large lags which increases the sensitivity to chance correlations (such as the peaks at lags −450 and +450 d).

successively longer variability time-scales and more extended flare shapes seen at longer cm bands. Furthermore, the correlation peak is close to time lag zero for the shortest wavelengths and shifts towards larger, positive (γ-ray leading) time lags with increasing radio wavelength. Finally, the correlation peak maxima increase towards the sub-mm band from $DCCF_{max} = 0.23 \pm 0.05$ at 110 mm to $DCCF_{max} = 0.61 \pm 0.05$ at 0.8 mm.

The estimated (source frame) time lags with uncertainties are shown in Fig. 5 as a function of radio frequency. The average time lag increases smoothly from 7 ± 9 d at 142 GHz (2 mm) to 76 ± 23 d at 2.6 GHz (110 mm). The errors given in Fig. 5 are total errors. Since the variability at different radio bands is usually correlated and the observing times were approximately the same in most cases, it follows that the errors in our lag estimates for the different bands are also correlated. Consequently, the lag uncertainty for one band relative to the other bands is smaller than implied by the error bars. This holds for all radio bands with the exception of the sub-mm APEX observations at 0.8 mm that were performed not simultaneous to the cm/mm bands and also include a slightly
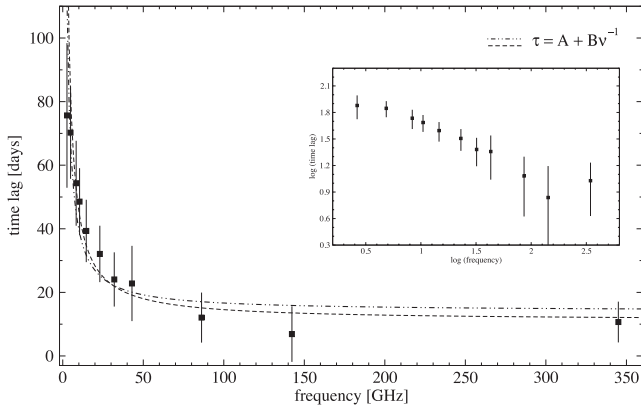
Figure 5. Stacked radio/γ-ray time lags (source frame) versus frequency. Positive lags denote γ-ray leading. A clear trend of decreasing lags towards higher frequencies is evident. The lines represent least-squares fits of the form $\tau_{r,\gamma}(\nu) = A + B\nu^{-1}$ to all lags (dash–dotted line) as well as omitting the lag of the lowest radio frequency (dashed line). For the former case, the fit parameters A and B are 14.1 and 257.4, respectively. The inset displays the data in a logarithmic representation.

different sample and a smaller number of sources. Although still consistent with the 2 mm band lag given our uncertainties, this likely also explains the slightly higher lag we obtain at 0.8 mm (11 ± 6 d) compared to 2 mm (7 ± 9 d).

5 DISCUSSION

5.1 Correlated radio/γ-ray variability and shocks

Several detailed previous and ongoing studies provide support for shocks (e.g. Marscher & Gear 1985; Türler 2011) as the origin of the observed radio variability in cm/mm band blazar light curves. Both detailed individual source and flare studies in the time and/or spectral domain (e.g. Marscher & Gear 1985; Türler, Courvoisier & Paltani 2000; Fromm et al. 2011; Orienti et al. 2013; Rani et al. 2013a) as well as studies of larger samples and/or many individual flares (e.g. Valtaoja et al. 1992; Stevens et al. 1994; Hovatta et al. 2008) often show an overall good agreement of the observed flare signatures with a shock-in-jet scenario. In particular, the multifrequency radio variability/flare amplitudes and time lags as well as the observed spectral evolution seen in the F-GAMMA radio data sets (i.e. the data also used in the present study) are in good agreement with the three stages of shock evolution for most of the sources (see Angelakis et al. 2011, in preparation; Orienti et al. 2013; Rani et al. 2013a; Fuhrmann et al. 2014; Nestoras et al., in preparation). Consequently, given the significant and strong radio/γ-ray correlations presented in Section 4.3, we conclude that the bulk γ-ray emission/variability is likely connected to the same shocked radio features. Those are first appearing and evolving in the innermost, ultracompact VLBI core region and subsequently moving downstream the jet at parsec scales with apparent superluminal speeds as seen in VLBI images. This is in line with similar conclusions of previous studies (e.g. Lähteenmäki & Valtaoja 2003; León-Tavares et al. 2011).

Assuming a leptonic emission scenario, the bulk γ-ray emission would then be produced in the shocks by IC up-scattering of ambient photons from the accretion disc, BLR, dusty torus and/or jet (synchrotron self-Compton) depending on the shock location and available ambient photon fields and their radiation energy densities (e.g. Ghisellini & Tavecchio 2009).

5.2 Radio opacity and the location of the γ-ray emitting region

Flare time delays in multifrequency radio light curves are often observed and commonly related to optical depth effects and travel time along the jet. The flare emission onsets and maxima appear typically first at the highest radio frequencies, i.e. in the 'mm VLBI core'. While subsequently moving downstream the jet and expanding adiabatically, they become observable and peak at successively lower frequencies where the optical depth of synchrotron self-absorption (SSA) τ_s (depending on the magnetic field and electron energy density) decreases to about unity at the given radio frequency.

Furthermore, radio opacity is also commonly observed as frequency-dependent 'core shifts' in multifrequency VLBI images (e.g. Lobanov 1998; Kovalev et al. 2008; Sokolovsky et al. 2011) with the core being identified as the most compact jet feature near the apparent base of the jet, and the surface at which the optical depth is ≈ 1 in a continuous jet flow (Blandford & Königl 1979). Assuming a conical jet geometry, the VLBI core absolute positions shift according to $r_{core} \propto \nu^{-1/k_r}$ where $k_r = [(3 - 2\alpha)m + 2n - 2]/(5 - 2\alpha)$. Here m and n denote the power-law exponents of the radial distance r-dependence of the magnetic field $B(r) \propto r^{-m}$ and the electron density $N(r) \propto r^{-n}$, and α denotes the optically thin spectral index (see Lobanov 1998), respectively. For SSA-dominated opacity and equipartition between jet particle and magnetic field energy density, k_r is 1 independent of the spectral index for the choice $m = 1$ and $n = 2$ (Königl 1981). In the presence of jet external density and pressure gradients and/or foreground free–free absorption (e.g. due to BLR clouds), k_r becomes >1 (e.g. Lobanov 1998). However, if the observed radio flare time lags are also due to opacity effects and the flare travels at a constant speed, we expect $\tau \propto \nu^{-1/k_r}$, accordingly. In this framework we examine the obtained radio/γ-ray time lag frequency dependence shown in Fig. 5. The data are well described (reduced $\chi^2 < 1$) by a power-law function of the form $\tau_{r,\gamma}(\nu) = A + B\nu^{-1}$ (see least-squares fits in Fig. 5), i.e. in good agreement with SSA-dominated opacity and equipartition ($k_r \simeq 1$).

Consequently, our results suggest a scenario where the γ rays escape instantaneously from the origin of the disturbance, whereas the radio emission from the same region becomes optically thin at progressively later times, i.e. flare maxima are observed successively delayed w.r.t. the γ-ray emission. A decreasing but still positive lag towards mm wavelength with e.g. $\tau_{3\,mm,\gamma} = 12 \pm 8$ d then strongly suggests that the bulk γ-ray production region is located inside and even upstream of the 3 mm core region. Towards higher frequencies the situation is less clear given the small lags and large uncertainties. At 2 mm wavelengths, for instance, the estimated lag is consistent with zero given our measurement uncertainties, possibly even indicating cospatial/contemporaneous emitting regions.

Using the average time lags we can estimate mean relative spatial offsets $\Delta r_{r,\gamma}$ between the region of γ-ray peak emission and the '$\tau = 1$ photosphere' of the various radio bands, given by

$$\Delta r_{r,\gamma} = \frac{\beta_{app} c\, \tau_{r,\gamma}^{source}}{\sin\theta}, \qquad (3)$$

with θ, β_{app} and $\tau_{r,\gamma}^{source}$ being the jet viewing angle, apparent jet speed (assumed to be constant) and the source frame radio/γ-ray time delay as obtained in Section 4.3, respectively.

Apparent jet speed measurements from the VLBI literature (e.g. Lister et al. 2009) are available for 42 sources in our sample. We note that the speed measurements used here are collected from non-contemporaneous VLBI observations. Recent studies show, however, that the dispersion of apparent speeds in a given jet is moderate and jet speeds cluster around a characteristic value (Lister

et al. 2013). Viewing angles have been estimated for these sources based on their β_{app} and variability Doppler factors calculated from the F-GAMMA radio data at 20 mm wavelength (Fuhrmann et al. 2014; Nestoras et al., in preparation; Angelakis et al., in preparation). Using the mean values of θ (6°.5) and β_{app} (17.5 c) for the 42 sources we obtain mean, de-projected radio/γ-ray distances decreasing from 9.8 ± 3.0 pc at 110 mm to 0.9 ± 1.1 and 1.4 ± 0.8 pc at 2 and 0.8 mm, respectively. The value of 5.1 ± 1.3 pc obtained at 20 mm is furthermore in good agreement with $\sim$7 pc obtained by Pushkarev et al. (2010) based on a comparable analysis using VLBI core flux densities at 20 mm. For individual sources showing significant 3 mm/γ-ray correlations we provide estimates of $\Delta r_{3mm, \gamma}$ in Table 3. The obtained values range between 0.2 and 15.9 pc.

5.3 Application to 3C 454.3

The good agreement of our estimated time lags with SSA-dominated opacity effects allows us to further constrain the location of the γ-ray emitting region for individual sources in our sample. To do so, we focus in the following on one particular source of Table 3, quasar J2253+1608 (hereafter 3C 454.3), and combine our previous results ($\Delta r_{3mm, \gamma}$) with SSA arguments and a radio/radio time lag analysis to obtain a lower limit for the distance of the γ-ray emitting region to the SMBH in this source.

Using the same DCCF analysis as in Section 3 to also obtain radio/radio time lags $\tau_{r,r}$ for all radio frequency combinations, we can estimate k_r and 'time lag core shifts' Δr_{mas} (see also Bach et al. 2006; Kudryavtseva et al. 2011) for 3C 454.3. The knowledge of k_r (usually obtained from VLBI core shifts at several frequencies) allows us to estimate the absolute distance of the radio $\tau = 1$ surface at a given frequency from the foot point of the jet (the 'jet base' or 'nozzle') according to $r_{base, \nu} = \Omega_{r, \nu}(\nu^{1/k_r} \sin\theta)^{-1}$. Here, $\Omega_{r, \nu} \propto \Delta r_{mas}(\nu_2^{1/k_r} - \nu_1^{1/k_r})^{-1}$ is a measure of the position offset at ν_1, ν_2 with $\nu_2 > \nu_1$ (see e.g. Lobanov 1998). Δr_{mas} denotes the angular offset $\Delta r_{mas} = \mu \cdot \tau_{r, r}$ with the VLBI jet proper motion $\mu = 0.3$ mas yr^{-1} observed for 3C 454.3 (Lister et al. 2009). At 3 mm wavelength we then obtain an absolute distance of the '$\tau = 1$ surface' from the jet base $r_{base, 3mm}$ of 1.8–2.6 pc.

A distance estimate of the γ-ray emitting region from the jet base $r_{base, \gamma}$ is then obtained using our previously estimated $\Delta r_{r, \gamma}$: $r_{base, \gamma} = r_{base, \nu} - \Delta r_{r, \gamma}$, whereas the distance to the central SMBH is given by $r_{BH, \gamma} = r_{BH, base} + r_{base, \gamma}$ with $r_{BH, base}$ being the distance between the black hole (BH) and the jet base. Using $\Delta r_{3mm, \gamma} = 1$ pc obtained for 3C 454.3 (Table 3) we estimate a distance $r_{base, \gamma}$ of 0.8–1.6 pc. Since the distance $r_{BH, base}$ is unknown (though likely small or negligible), the obtained value provides a lower limit for the distance of the γ-ray emitting region to the central SMBH in 3C 454.3. Given the typical BLR radii of $\lesssim$1 pc observed in AGN and an estimated value of $\sim$0.2 pc for the bulk BLR material in 3C 454.3 (Bonnoli et al. 2011), our analysis of 3C 454.3 reveals: (i) a 3 mm $\tau = 1$ surface ('core') well outside the canonical BLR, (ii) a location of the γ-ray emitting region upstream of the 3 mm core and at the outer BLR edge/extension or beyond. We note that the BLR of 3C 454.3 may be stratified and extend well beyond the canonical radius of $\sim$0.2 pc obtained from scaling relations. A more extended, parsec-scale structure in e.g. an 'outflowing BLR' scenario appears reasonable (see also León-Tavares et al. 2011). It is interesting to link our results to the recent findings of León-Tavares et al. (2013). These authors find BLR emission line variability in 3C 454.3 being powered by the non-thermal continuum emission of a new jet component traversing through the mm-band radio core implying that the latter is surrounded by BLR material. Given our

findings of the 'mm-core' being at $\sim$2–3 pc from the jet base well outside the canonical BLR radius thus supports the presence of BLR material even out to parsec-scale distances from the SMBH.

For a γ-ray emission location as obtained above, a leptonic scenario suggests either the BLR and its extension, the parsec-scale dusty torus and/or the jet as main sources of seed photons for IC up-scattering and bulk GeV photon production in 3C 454.3. A γ-ray location with weak accretion disc radiation but still a rich emission-line environment, i.e. the outer BLR, is in good agreement with recent modelling of the observed broad-band SEDs and γ-ray spectral breaks in this source using IC scattering of BLR photons and energy densities near equipartition (Cerruti et al. 2013).

6 SUMMARY AND CONCLUSIONS

We have presented first results of a detailed cross-correlation analysis between radio (cm, mm and sub-mm wavelengths of the F-GAMMA programme) and γ-ray variability in the $\sim$3.5 yr light curves of 54 *Fermi*-bright blazars. Our results for the studied sample can be summarized as follows.

(1) The 3.5 yr light curves often display strong outbursts (time-scales of months) and extended periods of activity (months to 1–2 yr) at both radio and γ rays, whereas the γ-ray variability usually appears to be more rapid.

(2) In order to increase the significance and sensitivity for correlations, a DCCF stacking analysis was performed using the whole sample and a new method to estimate correlation significances and chance correlations via a 'mixed source correlation' method. For the latter analysis, we used a total of 131 γ-ray light curves including additional 77 reference blazars. This yields for the first time strong, statistically significant multiband radio (11 cm to 0.8 mm) and γ-ray correlations. The radio emission is typically lagging the γ rays with sample average time lags ranging between 76 ± 23 and 7 ± 9 d, systematically decreasing from the longer cm wavelengths to the mm/sub-mm bands.

(3) The radio/γ-ray delay frequency dependence is well described by a power law $\tau_{r, \gamma}(\nu) \propto \nu^{-1}$, as expected for SSA dominated opacity effects (with $\tau \propto \nu^{1/k_r}$, $k_r \simeq 1$).

(4) Although the time lag rapidly decreases towards shorter wavelengths, a still positive delay at 3 mm with $\tau_{3mm, \gamma} = 12 \pm 8$ d suggests that the bulk γ-ray emission is coming from inside or even upstream of the (optically thick) 3 mm core region.

(5) The mean spatial distances between the region of γ-ray peak emission and the radio '$\tau = 1$ photosphere' are found to decrease from 9.8 ± 3.0 pc at 110 mm to 0.9 ± 1.1 and 1.4 ± 0.8 pc at 2 and 0.8 mm wavelength, respectively.

(6) Previous studies have shown that the multifrequency radio variability observed in our sample is in overall good agreement with shocks and their three-stage evolution. Given the strong radio/γ-ray correlations presented here, we thus conclude that the enhanced, bulk γ-ray emission is likely also connected to these shocked jet structures.

(7) We obtain 3 mm/γ-ray correlations for 9 individual sources at a significance level where we expect one occurring by chance (chance probability: 4×10^{-6}). These sources exhibit 3 mm/γ-ray time lags $\tau_{3mm, \gamma}$ in the source frame ranging between -4 ± 10 and 93 ± 16 d. No significant case of radio leading γ rays is found.

(8) The observed opacity/SSA effects allow us to further constrain the location of the γ-ray emitting region in individual sources using a new method which combines the radio/γ-ray as well as radio/radio time lags. Together with VLBI proper motion

measurements and assuming a conical jet, 'time lag core shifts' then reveal the absolute, de-projected distance of the bulk γ-ray emitting region from the jet base. Applied to 3C 454.3 we consequently obtain a lower limit for the γ-ray distance to the SMBH of 0.8–1.6 pc.

(9) For typical bulk BLR radii of $\lesssim$1 pc observed in AGN and a value of $\sim$0.2 pc obtained for 3C 454.3, we place the γ-ray emitting region in this source at the outer edge or beyond the BLR. Our finding of the $\tau = 1$ surface at 3 mm being at $\sim$2–3 pc from the jet base (i.e. well outside the canonical BLR) together with recent findings of León-Tavares et al. (2013) suggests that BLR material in 3C 454.3 extends to several parsec distances from the SMBH.

Our overall findings suggest a scenario where the bulk light-curve flare emission is produced in shocks moving down the jet, whereas the γ rays are escaping instantaneously from the shocked jet region and the optically thin radio emission from the same region reaches the observer successively delayed due to opacity effects and travel time along the jet. The current low detection rate of significant single-source correlations clearly demonstrates the need for longer data trains and a correspondingly better 'event statistic' to study the correlation properties and γ-ray location for a larger number of individual sources in detail. Our stacking analysis will furthermore enable more detailed studies of the radio/γ-ray correlation properties of the sample exploring possible differences of the correlation behaviour between different source classes (e.g. FSRQs versus BL Lacs) and testing dependences on different physical parameters such as BH mass, BLR size, luminosity, jet opening angle and Doppler factor (Fuhrmann et al., in preparation; Larsson et al., in preparation).

We stress that the overall situation is complex. The strong and significant multiband correlations presented here are statistical in nature and often no simple, detailed one-to-one correlation of single radio and γ-ray flares is observed. In addition, our correlation method and data sets are mostly sensitive to the maxima and minima of the most prominent, long-term variability/flares in the studied sample. The radio/γ-ray correlation properties of the more rapid γ-ray flares often observed in these sources on time-scales of $\lesssim$hours or days to a few weeks (and not resolved with our data sets and analysis) may be different. These events may be produced also at different locations. However, the very smooth and continuous behaviour of the observed time lag in agreement with SSA all the way to the mm and sub-mm bands may provide some evidence against the '43 GHz standing shock and turbulent extreme multizone scenario' (e.g. Marscher & Jorstad 2010; Marscher 2014). Future, more detailed studies of single sources will shed further light on this topic.

Neither our stacking method nor single-source results provide strong evidence for cases of radio leading γ rays. This demonstrates the limited predictive power of radio flares to reliably trigger *Fermi* observations of flaring γ-ray sources (whereas the detection of a γ-ray flare by *Fermi* likely signals an impending high state at radio bands). This statement holds unless radio (mm/sub-mm) flare onsets occur simultaneously with or even before γ-ray flare onsets, which is unclear at the moment. This needs to be addressed in future studies.

ACKNOWLEDGEMENTS

REFERENCES

Abdo A. A. et al., 2010a, Nature, 463, 919
Abdo A. A. et al., 2010b, ApJ, 722, 520
Ackermann M. et al., 2011, ApJ, 743, 171
Agudo I. et al., 2011a, ApJ, 726, L13
Agudo I. et al., 2011b, ApJ, 735, L10
Angelakis E., Fuhrmann L., Nestoras I., Zensus J. A., Marchili N., Pavlidou V., Krichbaum T. P., 2010, preprint (arXiv:1006.5610)
Angelakis E. et al., 2011, preprint (arXiv:1111.6992)
Bach U. et al., 2006, A&A, 456, 105
Blandford R. D., Königl A., 1979, ApJ, 232, 34
Blandford R. D., Levinson A., 1995, ApJ, 441, 79
Bonnoli G., Ghisellini G., Foschini L., Tavecchio F., Ghirlanda G., 2011, MNRAS, 410, 368
Böttcher M., Reimer A., Marscher A. P., 2009, ApJ, 703, 1168
Cerruti M., Dermer C. D., Lott B., Boisson C., Zech A., 2013, ApJ, 771, L4
Dermer C. D., Cerruti M., Lott B., Boisson C., Zech A., 2014, ApJ, 782, 82
Dotson A., Georganopoulos M., Kazanas D., Perlman E. S., 2012, ApJ, 758, L15
Edelson R. A., Krolik J. H., 1988, ApJ, 333, 646
Finke J. D., Dermer C. D., 2010, ApJ, 714, L303
Foschini L., Tagliaferri G., Ghisellini G., Ghirlanda G., Tavecchio F., Bonnoli G., 2010, MNRAS, 408, 448
Fromm C. M. et al., 2011, A&A, 531, 95
Fuhrmann L., Zensus J. A., Krichbaum T. P., Angelakis E., Readhead A. C. S., 2007, in AIP Conf. Proc. 921, The First Glast Symposium. Am. Inst. Phys., New York, p. 249
Fuhrmann L. et al., 2008, A&A, 490, 1019
Fuhrmann L. et al., 2014, A&A, submitted
Ghisellini G., Tavecchio F., 2009, MNRAS, 397, 985
Hovatta T., Nieppola E., Tornikoski M., Valtaoja E., Aller M. F., Aller H. D., 2008, A&A, 485, 51
Jorstad S. G., Marscher A. P., Mattox J. R., Aller M. F., Aller H. D., Wehrle A. E., Bloom S. D., 2001, ApJ, 556, 738
Jorstad S. G. et al., 2010, ApJ, 715, 362
Jorstad S. G. et al., 2013, ApJ, 773, 147
Königl A., 1981, ApJ, 243, 700

Kovalev Y. Y., Lobanov A. P., Pushkarev A. B., Zensus J. A., 2008, A&A, 483, 759

Kovalev Y. Y. et al., 2009, ApJ, 696, L17

Kudryavtseva N. A., Gabuzda D. C., Aller M. F., Aller H. D., 2011, MNRAS, 415, 1631

Lähteenmäki A., Valtaoja E., 2003, ApJ, 590, 95

Larsson S., 2012, preprint (arXiv:1207.1459v1)

Larsson S. et al., 2012, preprint (arXiv:1206.3799)

León-Tavares J., Valtaoja E., Tornikoski M., Lähteenmäki A., Nieppola E., 2011, A&A, 532, 146

León-Tavares J. et al., 2013, ApJ, 763, L36

Lister M. L. et al., 2009, ApJ, 138, 1874

Lister M. L. et al., 2013, ApJ, 146, 120

Lobanov A. P., 1998, A&A, 330, 79

Marscher A. P., 2014, ApJ, 780, 87

Marscher A. P., Gear W. K., 1985, ApJ, 298, 114

Marscher A. P., Jorstad S. G., 2010, preprint (arXiv:1005.5551)

Marscher A. P. et al., 2010, ApJ, 710, L126

Max-Moerbeck W. et al., 2013, preprint (arXiv:1303.2131)

Nolan P. L. et al., 2012, ApJS, 199, 31

Orienti M. et al., 2013, MNRAS, 428, 2418

Peterson B. M., Wanders I., Horne K., Collier S., Alexander T., Kaspi S., Maoz D., 1998, PASP, 110, 660

Poutanen J., Stern B., 2010, ApJ, 717, L118

Pushkarev A. B., Kovalev Y. Y., Lister M. L., 2010, ApJ, 722, L7

Raiteri C. M. et al., 2013, MNRAS, 436, 1530

Rani B. et al., 2013a, A&A, 552, 11

Rani B., Lott B., Krichbaum T. P., Fuhrmann L., Zensus J. A., 2013b, A&A, 557, 71

Schinzel F. K., Lobanov A. P., Taylor G. B., Jorstad S. G., Marscher A. P., Zensus J. A., 2012, A&A, 537, 70

Sokolovsky K. V., Kovalev Y. Y., Pushkarev A. B., Lobanov A. P., 2011, A&A, 532, 38

Stern B. E., Poutanen J., 2011, MNRAS, 417, L11

Stevens J. A., Litchfield S. J., Robson E. I., Hughes D. H., Gear W. K., Teräsranta H., Valtaoja E., Tornikoski M., 1994, ApJ, 437, 91

Tavecchio F., Ghisellini G., 2012, preprint (arXiv:1209.2291v1)

Tavecchio F., Ghisellini G., Bonnoli G., Ghirlanda G., 2010, MNRAS, 405, L94

Türler M., 2011, Mem. Soc. Astron. Ital., 82, 104

Türler M., Courvoisier T. J. L., Paltani S., 2000, A&A, 361, 850

Valtaoja E., Teräsranta H., 1995, A&A, 297, L13

Valtaoja E., Teräsranta H., Urpo S., Nesterov N. S., Lainela M., Valtonen M., 1992, A&A, 254, 71

Wehrle A. E. et al., 2012, ApJ, 758, 72

White R. J., Peterson B. M., 1994, PASP, 106, 879

SUPPORTING INFORMATION

Additional Supporting Information may be found in the online version of this article:

Table 2. List of selected sources included in the current analysis (http://mnras.oxfordjournals.org/lookup/suppl/doi:10.1093/mnras/stu540/-/DC1).

Please note: Oxford University Press are not responsible for the content or functionality of any supporting materials supplied by the authors. Any queries (other than missing material) should be directed to the corresponding author for the paper.

This paper has been typeset from a TEX/LATEX file prepared by the author.